PNAS INAUGURAL ARTICLE | EARTH, ATMOSPHERIC, AND PLANETARY SCIENCES OPEN ACCESS

Prince Rupert's Drops: An analysis of fragmentation by thermal stresses and quench granulation of glass and bubbly glass

Katharine V. Cashman[a,1], Emma J. Liu[b], and Alison C. Rust[c]

This contribution is part of the special series of Inaugural Articles by members of the National Academy of Sciences elected in 2016.
Contributed by Katharine V. Cashman; received February 16, 2022; accepted May 4, 2022; reviewed by Munawar Chaudhri and Michael Manga

When volcanic eruptions involve interaction with external water (hydrovolcanism), the result is an ash-rich and energetic volcanic plume, as illustrated dramatically by the January 2022 Tonga eruption. The origin of the high explosive energy of these events remains an important question. We investigate this question by studying Prince Rupert's Drops (PRDs)—tadpole-shaped glass beads formed by dripping molten glass into water—which have long fascinated materials scientists because the great strength of the head contrasts with the explosivity of the metastable interior when the tail is broken. We show that the fragment size distribution (FSD) produced by explosive fragmentation changes systematically with PRD fragmentation in air, water, and syrup. Most FSDs are fractal over much of the size range, scaling that can be explained by the repeated fracture bifurcation observed in three-dimensional images from microcomputed tomography. The shapes of constituent fragments are determined by their position within the original PRD, with platey fragments formed from the outer (compressive) shell and blocky fragments formed by fractures perpendicular to interior voids. When molten drops fail to form PRDs, the glass disintegrates by quench granulation, a process that produces fractal FSDs but with a larger median size than explosively generated fragments. Critically, adding bubbles to the molten glass prevents PRD formation and promotes quench granulation, suggesting that granulation is modulated by heterogeneous stress fields formed around the bubbles during sudden cooling and contraction. Together, these observations provide insight into glass fragmentation and potentially, processes operating during hydrovolcanism.

glass | fragmentation | Prince Rupert's Drops

Significance

Understanding the fracture and fragmentation of amorphous materials is important for disciplines that span from glass technology to volcanology. Prince Rupert's Drops can be viewed as small-scale experiments that provide links between internal stress distributions, patterns of fracture propagation, and resulting fragment sizes and shapes. These links provide key information for forensic analysis of the products of fragmentation and help to anticipate the fragmentation behavior of glassy materials that have experienced different cooling histories (for example, in volcanic eruptions).

> Honour is like that glassy bubble
> That finds philosophers such trouble.
> Whose least part crack'd, the whole does fly,
> And wits are crack'd, to find out why —Samuel Butler (Hudibras, Part II, Canto II, lines 385–389, 1664)

Prince Rupert's Drops (PRDs), also known as Batavian tears because of their early production in Holland, are known for their unusual fracture properties; the head is very strong, but the entire drop will shatter explosively if the tail is broken. These properties are caused by internal residual stresses—a strong compressive outer layer surrounding an interior under tension—produced during rapid quenching of molten glass droplets in water. PRDs have been of interest to natural philosophers and materials scientists for centuries because of their strength (1–3). For example, glass created with a strong outer compressive layer has been used to construct lead shot (4) and toughen glass for automobile windshields or more recently, transparent armor (5). Our interest in PRDs comes from the perspective of physical volcanology and long-standing questions about the behavior of magma when it interacts with external water. Magma–water interaction has been modeled using concepts of molten fuel coolant interaction from the nuclear industry (6–11). Recent studies have further suggested that magma–water interaction in many hydrovolcanic volcanic eruptions may involve mixing with a water–sediment slurry instead of pure water (12–15) and that thermal contraction and quench granulation may play an important role in generating the fine-scale fragmentation that is a common result of magma–water interaction (16–20). Neglected by most volcanological studies, however, are details of fracture initiation and propagation or importantly, the role of bubbles in enhancing quench granulation despite evidence that, in many hydrovolcanic eruptions, the magma was highly vesicular (bubbly) when it encountered external water (15, 19).

Here, we use this volcanological perspective to explore environmental controls on fragmentation, fracture propagation, and the resulting fragment populations created

Author affiliations: [a]Department of Earth Science, University of Oregon, Eugene, OR 97405; [b]Earth Sciences, University College London, London WC1E 6BS, United Kingdom; and [c]School of Earth Sciences, University of Bristol, Bristol BS8 4YA, United Kingdom

Author contributions: K.V.C. and A.C.R. designed research; K.V.C., E.J.L., and A.C.R. performed research; E.J.L. contributed new reagents/analytic tools; K.V.C., E.J.L., and A.C.R. analyzed data; and K.V.C., E.J.L., and A.C.R. wrote the paper.

Reviewers: M.C., Cambridge University; and M.M., University of California, Berkeley.

Competing interest statement: Reviewer M.M. and author K.V.C. were coauthors on a review article published in *Nature Communications*: in 2018: M. Cassidy, M. Manga, K. Cashman, O. Bachmann, Controls on explosive-effusive volcanic eruption styles. *Nature Commun* DOI: 10.1038/s41467-018-05293-3. 9, 2893 (2018).

[1]To whom correspondence may be addressed. Email: cashman@uoregon.edu.

See Profile, e2210776119, in vol. 119, issue 31.

This article contains supporting information online at http://www.pnas.org/lookup/suppl/doi:10.1073/pnas.2202856119/-/DCSupplemental.

Published July 21, 2022.

by both explosive fragmentation and quench granulation of bubble-bearing and bubble-free molten glass. We use PRDs to study these processes because they provide a manageable way to study glass fragmentation; we do not suggest that PRDs form during volcanic eruptions. In this study, we focus particularly on the size and shape characteristics of the fragments produced, attributes that are commonly used to characterize volcanic ash fragments. We measure fragment size and shape distributions by sieving and analysis of microcomputed tomography (μCT) images. We conclude that the fragment size distribution (FSD) created by explosive fragmentation depends on the medium in which a PRD is broken in addition to physical characteristics of the drop (size, shape, and internal voids), that individual fragment shapes vary with location within the drop, and that quench granulation (melt disintegration without PRD formation) creates power law FSDs and is the sole response of an interaction between water and bubbly molten glass. The latter observation supports inferences from volcanological studies on the potential importance of bubbles in promoting highly explosive magma–water interaction.

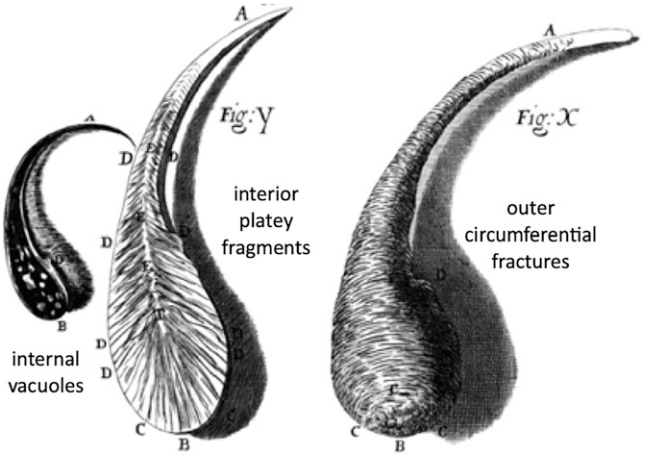

Fig. 1. From Hooke's (1665) *Micrographia*. Note the internal bubbles in the small drop in *Left* as well as the conical cracks revealed in the cross-section (Fig. *Y*) and the intersection of these cracks with the PRD surface to form circumferential fractures (Fig. *X*). Reproduced with permission from the Royal Society.

PRDs: Background

The history and early scientific theories of PRDs are reviewed in ref. 1; their place in court entertainment and in the history of natural philosophy are described in refs. 2 and 3. These glass beads were first documented in Mecklenburg, Germany, sometime before 1625, although the method of strengthening glass by rapid quenching may have been known since Roman times. Prince Rupert of Bavaria, who introduced them to the court of King Charles II in 1660, sought an explanation for their formation from Gresham College (later the Royal Society).

The most comprehensive early study of PRDs was by Hooke, who presented detailed observations of their fracture properties in his *Micrographia* (1665; https://royalsociety.org/collections/digital-resources/). Hooke employed a range of experimental techniques to develop conjectures about PRDs, including grinding to determine the thickness of the strong outer layer, encasing a drop to retain the broken pieces for study, and determining changes in the physical properties of liquids during heating and cooling. From this work, he correctly asserted that hot fluids are more expanded than cooler fluids, that fluids contract on cooling, that quenching creates a force on the outer glass layer that provides the energy for rapid fragmentation when released, and that annealing prevents explosive fragmentation. Hooke was incorrect, however, in inferring that the outer surface was in tension (it is in compression). Hooke also described surface fractures in the form of partial circumferential ring cracks, which he hypothesized to be conical cracks with apexes orientated toward the tail of the drop and caused by the release of internal tension (Fig. 1). PRD research in the nineteenth century added descriptions of internal voids, confirmed their origin by contraction, and demonstrated that they were under vacuum (21).

It is the unusual strength properties of PRDs that make them so intriguing; the head of the drop can withstand a force of 15 kN (22), yet the tail, broken with simple finger pressure applied over the small cross-sectional area of the tail, causes the entire drop to disintegrate explosively to a fine powder. The accepted explanation for these properties is that the exterior is in a state of compression, while the interior is in tension (22, 23). Glass contracts on cooling at a speed dependent on the cooling rate and by an amount determined by the specific properties of the silicate melt. Quenching in water produces differential cooling rates through the thickness of a drop, such that rapid chilling of the exterior forms a solid outer shell while the core remains molten. Subsequent cooling of the interior causes the core to contract, producing the observed residual stress field. Soda lime glass, in particular, has optimal properties for PRD formation because of its relatively low melting temperature and high coefficient of thermal expansion (22).

The high compressive stresses in the exterior shell, together with the hemispherical morphology, explain PRD strength. Breaking the PRD tail exposes the tensile core and initiates a fracture wave [or failure wave (5)] that propagates rapidly toward the head of the drop from the point of failure. High-speed photography (22, 24–26) shows that the fracture wave velocity in soda lime glass is 1,700 ± 100 ms^{-1}. The velocity in lead oxide glass is significantly slower (1,300 ± 100 ms^{-1}) and illustrates the influence of glass structure on the dynamics of fracture propagation. The fracture wave itself is self-sustaining, driven by the release of potential energy stored within the glass atomic structure. The wave propagation velocity is constant and independent of distance from the point of failure (27). Although voids distort the local stress field, they do not affect the fragmentation speed. Individual fragments are dispersed outward only after the fracture wave has passed completely through the drop (22).

Individual fractures appear to propagate by means of bifurcating cracks (24). Unclear is whether the velocity of the fracture wave is limited by the terminal velocity of individual fractures (22) or whether self-propagating fracture fronts move at characteristic velocities that exceed normal maximum crack speed (5). Observations of impact-generated cracks in thermally tempered glass suggest that both the speed and the style of fracture propagation in PRDs change as the front passes from the tensional into the compressional regime at the drop head. Specifically, crack propagation slows dramatically (from ∼1,500 m/s to 200 to 300 m/s) on entering the compressive surface layers (28); crack bifurcation also ceases at this point (22).

The exact mechanism responsible for crack propagation in PRDs (29, 30) and more generally, in glass fracture (31) remains an active topic of research. A theoretical foundation is supplied by Griffith crack theory and the broader field of fracture mechanics (32, 33). Energy for creating new surface area is acquired from the internal elastic energy of the surrounding

medium, but only if 1) the stress field around the crack is tensile and 2) the product of the stress and the square root of the crack diameter exceeds a material-dependent critical parameter. As a result, microcracks in the outer (compressive) PRD surface cannot grow until that stress is released. Patterns of crack propagation also control the shape of individual fragmented particles. Ordinary tempered glass breaks into cubes. Fragments formed by PRDs, in contrast, typically form platelets (5, 34), although some are needle like and many have surface striations (22). The origin of these particle forms has not been determined explicitly. Indeed, it has been suggested that "the next step to answer this puzzle would be to investigate drops, exploded within some sort of confining matrix to permit statistical analysis of fragments drawn separately from areas of tension and compression" (35).

PRD Formation and Internal Stresses

PRDs form when molten glass is dripped into cold water. We made both small PRDs (~1 g; from soda lime glass) and large PRDs (~20 g; from lead oxide glass) (*Materials and Methods*). Importantly, not all attempts to make PRDs are successful as some pours disintegrate when the molten glass hits the water; we refer to this as quench (thermal) granulation. Fragments produced by quench granulation provide reference particles for nonexplosive fragmentation (that is, fragmentation not driven by excess internal stress). We also experimented with molten glass to which bubbles were added. Importantly, we could not make PRDs from the bubbly melt, which always experienced quench granulation. Disintegration is also immediate when PRDs are dropped into liquid nitrogen (22). Together, these observations suggest that there are optimal cooling rates and melt properties for PRD formation.

Intact PRDs vary in overall morphology from drops that are straight with straight tails to those that are curved with curly tails (Fig. 2 and *SI Appendix*, Fig. S1). The morphology is controlled by the specific conditions of quenching as the molten glass is dripped into the water. The degree of curvature of the tail, for example, is determined by the way in which the drop enters the water (4). If the stream of melt enters the water at an oblique angle, quenching will be faster on the underside, which deforms the drop. More generally, the speed and temperature of water motion relative to the outer surface of the drop control both quench conditions and the spatial distribution of the cooling rate, hence the geometry and magnitude of stored stresses. Cooling-driven contraction of the core forms interior voids, which disappear when PRDs of soda lime glass are annealed at 700 °C (23). Such voids are common in volcanic samples where small amounts of melt trapped within crystals (melt inclusions) contract during rapid (eruption-related) cooling, where they are referred to as "shrinkage bubbles" (36); importantly, they act to relieve stresses caused by contraction of the melt across the glass transition.

We found only rare cases of void-free small PRDs (Fig. 2 *B* and *C*) and no void-free large PRDs. Internal voids in small PRDs are near spherical in the head and spherical to elongated in the tail (Fig. 2 *A* and *D*–*F*). PRDs with straight tails contain at most one or two large voids within the head region, while those with curved tails often show a train of smaller voids extending from the center of the head down the tail (Fig. 2*A*). These void trains are not arranged axisymmetrically but instead, are displaced toward the outer surface of the curvature of the tail, consistent with rapid cooling of the underside of curved drops, which leaves the void train to mark the last volume to cool and cross the glass transition. Large PRDs contain a range of void sizes and shapes from a single void running through the head to voids distributed throughout the head and tail.

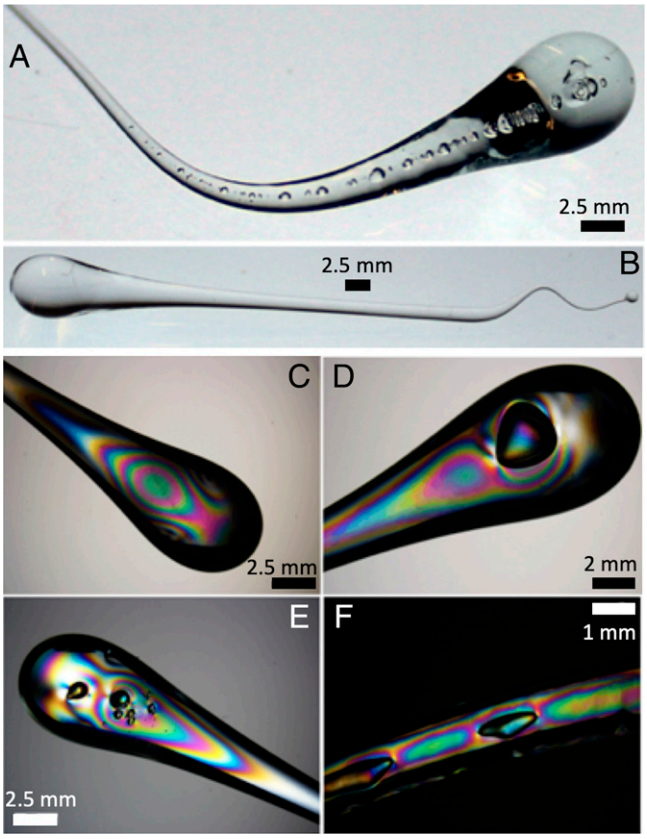

Fig. 2. Microscope images of small PRDs. *A* and *B* are binocular images of bubble-bearing (*A*) and bubble-free (*B*) PRDs. *C*–*F* are cross-polarized images of small PRDs obtained by photographing through polaroid sheets. (*C*) Polarization interference colors in a PRD that lacks an internal void. (*D*–*F*) Distortion of the stress field (shown as distortion of the polarization fringes) caused by (*D*) a single bubble in the head, (*E*) multiple bubbles in the head, and (*F*) multiple bubbles in the tail.

The internal distribution of stresses can be visualized using crossed polarizers (Fig. 2 *C*–*F*). A small void-free PRD has a symmetrical stress distribution (Fig. 2*C*). Single or multiple voids in the head and tail distort the local stress field, with larger voids causing more severe distortion (Fig. 2*D*) and multiple voids creating complex stress fields (Fig. 2 *E* and *F*). It has been suggested that the number of voids increases with the glass expansion coefficient (4) and that in soda lime glass specifically, shrinkage bubbles (voids) comprise 1 to 2 vol % of the PRD (34). In our experience, however, both the number and volume of voids vary in PRDs of the same composition. Moreover, although controls on the specific location, size, and number of individual voids are not well understood, it seems likely that their distribution is determined by specific patterns of cooling. Finally, the absence of void space may record cooling rates at the margin of those required to form PRDs.

The magnitudes of internal stresses have been quantified. An early study of soda lime glass PRDs (~6-mm-diameter head) measured surface compressive and axial tensional stresses ≤170 MPa and a tensile zone encompassing 70% of the head (4, 22). A more recent study of slightly larger (head diameter ≤7.8 mm) soda lime glass PRDs analyzed polarized images to determine compressive stresses of ~525 MPa (head) and 700 MPa (tail), with tensile stresses in the interior of 300 to 400 MPa (23) (Fig. 3). The same study shows the thickness of

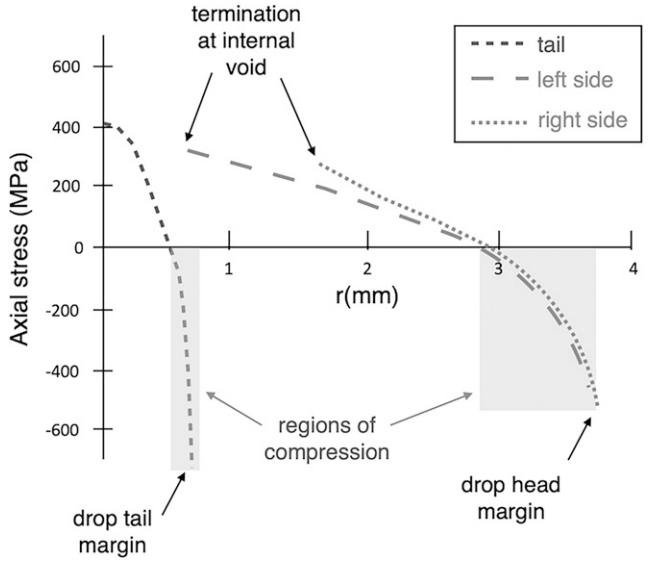

Fig. 3. Axial stresses within a PRD illustrate the large compressive stresses (negative) along the outer surface of the drop and large tensile stresses (positive) in the drop interior. Gray shaded areas show the thickness of compressive layers. Adapted from ref. 23.

the surface compressive layer to be 0.5 to 0.85 mm (gray shaded areas in Fig. 3), which is similar to earlier estimates where the thickness was measured by progressive etching with acid (4). Fig. 3 also shows the asymmetry of tensile stresses in the PRD head caused by the asymmetric location of the internal void.

Effect of the Confining Medium on PRD Fragmentation

As known for centuries, PRDs fragment explosively when the compressive surface layer is disrupted by breaking the tail. The velocity of the fracture wave is independent of both the confining medium (i.e., air, water, or glycerol) that surrounds the ambient temperature PRD when broken and the drop head diameter [validated for drops of 6- to 8-mm maximum head diameter (27)]. Less is known about the effect of the confining medium on patterns of fragmentation, except that a high-viscosity medium reduces dispersion of individual fragments (22).

To examine the role of the confining medium on fragmentation behavior, we broke both small and large PRDs either encased in solid epoxy or immersed in Newtonian fluids of different viscosity: air ($\sim 10^{-5}$ Pa s), water ($\sim 10^{-3}$ Pa s), golden syrup (~100 Pa s), and hair gel (non-Newtonian, used for μCT experiments) (*SI Appendix*, Table S1). All PRDs were initially formed by quenching in water. Fig. 4*A* shows FSDs for four to five individual large PRDs broken in each of the three Newtonian fluids. The median grain size increases from ~1 mm for fragmentation in air to ~2 mm for fragmentation in syrup. The same is true of the small PRDs, although the FSDs are displaced to smaller sizes (Fig. 4*B*). FSDs determined by analysis of μCT reconstructions of a small PRD fragmented in hair gel are shown for comparison in Fig. 4*B*. Importantly, the μCT reconstructions allow us to analyze the distribution of individual fragment volumes; to compare these data with sieve measurements, we convert mass to volume using the known glass density (2.5 g/cm^3) and assign individual fragments to size classes for both cubic (L^3) and platey ($L \times L \times L/5$) shapes, where L refers to the length in one dimension. Overall, the μCT experiments produce size distributions that are similar to, or finer grained than, PRD fragmentation in air, assuming that nonisotropic fragment shapes move the distribution to larger effective sizes.

The variation in FSD with confining medium demonstrates that internal stresses are not the only control on PRD fragmentation. Instead, our observations suggest that the crack propagation responsible for creating individual fragments is modulated by the ability of cracks to separate (expand) as they form. Evidence of crack expansion prior to drop disintegration is provided by examination of μCT cross-sections of epoxy-encased PRDs (*SI Appendix*, Fig. S2). Here, fractures do not traverse the outermost compressive shell, demonstrating that the glass drop as a whole did not reach the point of disintegration. Nonetheless, the gaps opened by fractures comprise 3 to 5% of the cross-sectional area, evidence that crack formation requires expansion to accommodate displacement of individual fragments (37). In the epoxy-encased μCT experiments, this volume increase must have been accommodated by expansion of the epoxy and/or by fragment displacement into the internal voids. Indeed, a void-free epoxy-encased PRD failed to fragment, perhaps because it lacked internal accommodation space.

Recent PRD studies (29, 34, 38) have investigated the fracture properties of PRDs by measuring FSDs. These studies have reached different conclusions, however, with FSDs reported as either fractal (29) or exponential (34, 38); no attempt has been made to relate patterns of fracture to the characteristics of the resulting fragments or the presence of interior voids, and all prior work assumes that fracture patterns are determined entirely by the retained internal stresses. We test both fractal (power law) and exponential models using data from large PRDs fragmented explosively (13 samples, ~20 g each). By measuring the FSD of individual PRDs broken in the same medium, we evaluate the variability in FSD caused by different PRD shapes and void distribution. By comparing FSDs from PRDs explosively fragmented in different media, we examine the possible effect of the fragmentation environment on the fragmentation process.

We first follow ref. 29 in using a mass-based assessment of fractal dimension (D_m) appropriate for sieve-based measurements:

$$\frac{d\log M(L)}{d\log(L)} = 3 - D_m, \qquad [1]$$

where $M(L)$ is the cumulative mass distribution ($M < L$). We find that most FSDs produced by explosive fragmentation have log$L$ vs. log$M < L$ relations that can be fit by a power law for fragments with $L \leq 2$ mm and that account for a mass fraction of >0.6 (Fig. 5 *A* and *B*). Data for individual PRDs span a D_m range from −0.09 to 1.95, which encompasses the D_m values of 1.06 ± 0.09 reported by ref. 29 for the combined fragments of ~50 lead crystal PRDs broken in air and approaches $D_m \geq 2$ typical of brittle materials (39). As anticipated from the cumulative plots shown in Fig. 4 *A* and *B*, log–log plots of mass fraction and particle size also vary with surrounding medium. Of the individual groups, PRDs fragmented in air have the highest average $D_m = 1.59$, reflecting the small median fragment size of this group (Fig. 4*C*). A single outlier (D_m =1.08) has a large void between the head and tail (*SI Appendix*, Fig. S1) that may have limited fracture propagation into the head; this would explain both the large maximum fragment size (>8 mm) and the poor fit to the power law plot. PRDs fragmented in syrup show both pronounced curvature (poor power law fits) and low D_m values ($D_m = -0.09$ to 0.38). PRDs fragmented in water have the smallest D_m range ($D_m = 1.31$ to 1.45) and the best

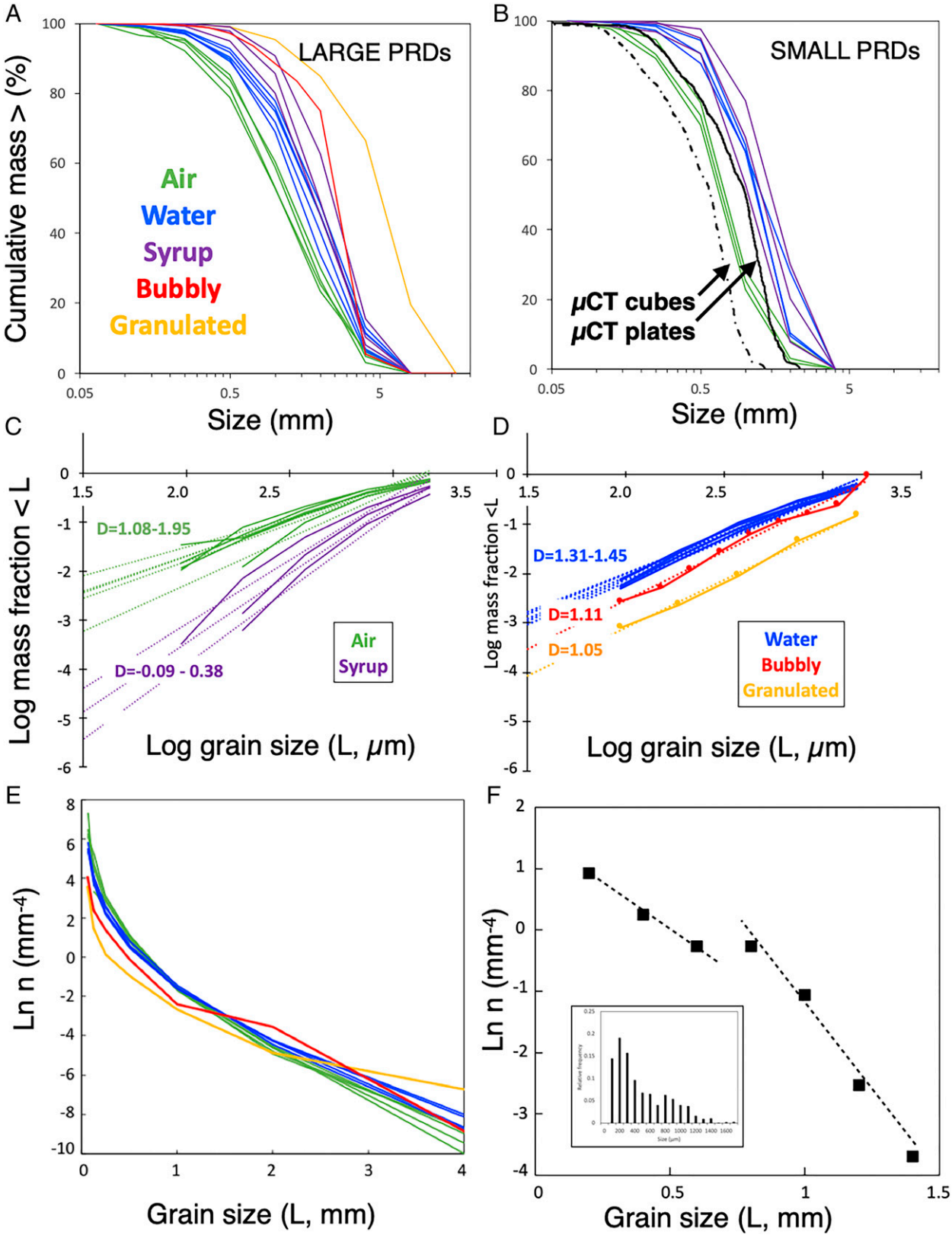

Fig. 4. PRD FSDs. (*A*) Large (~20-g) PRDs. Colors denote the mediums of fragmentation (air, water, syrup) for explosively fragmented particles; each line represents a single fragmented particle. FSDs created by quench granulation of both pure (orange) and bubbly (red) melt are combined fragments for quench granulation experiments. (*B*) FSDs for small (~1-g) PRDs (same color scheme as used for large PRDs) and measurements from the μCT hair gel experiment, where fragment volume measurements (*V*) are converted to effective sieve size (*L*) assuming either cubes ($L = V^{1/3}$) or plates [$L = (5 \times V)^{1/3}$]. (*C* and *D*) Fractal analysis of glass fragments separated into two groups—(*C*) PRDs explosively broken in air or syrup and (*D*) PRDs explosively broken in water and fragments produced by quench granulation of bubbly and bubble-free samples. (*E*) FSDs based on number density distributions of samples explosively fragmented in air and syrup. The curve fit for the most linear syrup FSD yields a slope used to calculate dominant size L_D. (*F*) FSDs for μCT data plotted as both an exponential distribution and histogram to illustrate bimodality.

fits (are closest to linear on a log–log plot) (Fig. 4*D*). Excellent power law fits are also found for the products of quench granulation, both bubble bearing and bubble free. Analysis of individual fragment volumes (D_v) measured from μCT images (PRD in hair gel) yields a cumulative curve with two offset linear segments ($D_v = 0.05, 0.14$) (*SI Appendix*, Fig. S3).

For FSDs that showed some deviation from power law fits, we also checked for exponential distributions by calculating fragment number density distributions $n(L)$, defined as the number of particles per unit volume (V) per size class (Fig. 4*E*). An exponential FSD would form a straight line in a plot of ln (n) vs. L. For simplicity, we assume that $L = V^{1/3}$, which does not account for variable fragment shape or size definitions (40). Large PRDs fragmented explosively in air yield $n(L)$ vs. L plots that are concave upward (Fig. 4*E*). These trends are expected for power law (fractal) distributions; they also resemble the two-slope power law trends reported by refs. 34 and 38 for PRD fragmentation in air but lack the clear break in slope apparent in their data. It is possible that our data, obtained by sieving, lack sufficient resolution to identify a discrete slope break and that the air-fragmented PRDs could be fit by two exponential curves, although examination of Fig. 5*A* suggests that FSDs from individual PRDs can form either an exponential or power law distribution depending on geometry and internal voids. PRDs fragmented explosively in syrup, in contrast, are well fit by an exponential distribution. Data from μCT analysis of the PRD fragmented in hair gel can be fit with two offset lines on an exponential plot; when plotted as a histogram, these data show two discrete maxima (Fig. 4*F*).

What Do FSDs Tell Us about Explosive Fragmentation of PRDs?

Fractal dimensions measure the change in mass (or volume or number) of particles as a function of size. A D_m of zero means that each size class contains the same particle mass; D_m is greater than zero when the smaller size classes contain more mass than the larger size classes. D_m thus provides a measure of fragmentation efficiency. By this metric, explosive fragmentation is more efficient for PRDs fragmented in air than for PRDs fragmented in syrup. This is interesting because PRDs of a similar size and glass composition should have approximately the same internal stresses (Fig. 3), which means that differences in fragmentation efficiency reflect not only the internal stresses but also, the properties of the confining medium.

Fragmentation is controlled by the geometry of fracture propagation. Imaging of fragmentation waves formed during explosive disintegration of PRDs shows that fracture propagation is sequential from the tail to the head and involves crack bifurcation (24, 26), a consequence of the speed of the high-energy release

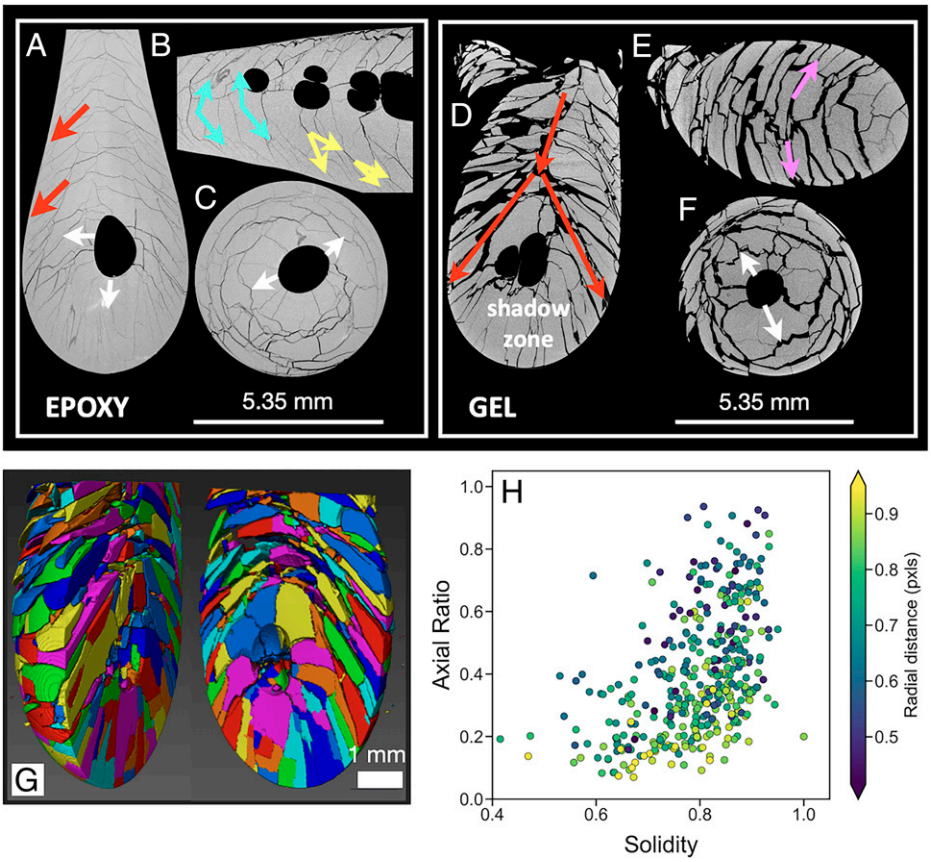

Fig. 5. Cross-sectional images through μCT reconstructed volumes. (*A–C*) Epoxy-encased PRDs. (*A*) Longitudinal section of PRD2 with a single internal bubble. (*B*) Longitudinal section of PRD3 with multiple bubbles. (*C*) Horizontal section of PRD2 (*SI Appendix*, Fig. S2). (*D–F*) Gel-encased PRD4. (*D*) Longitudinal section. (*E*) View of the outer surface. (*F*) Horizontal section. Red arrows indicate the direction of fracture propagation. White arrows highlight the radial perpendicular fractures associated with interior bubbles. Yellow arrows show acute branching. Turquoise arrows show oblique branching. Pink arrows show intersections of fractures with PRD exterior. (*G*) Rendering of individual fragments within the Carbopol-encased PRD4. Note the abrupt change in shape from the interior blocky fragments around the interior void and the surrounding platey fragments. Smaller fragments can be seen throughout wherever fractures intersect. (*H*) Quantifying fragment shapes using 2D (near-horizontal) cross-sections of μCT scans. Here, we use the axial ratio (short axis/long axis, where a value of one represents a fully equant form) to measure elongation and solidity (fragment area/area of convex hull, where a value of one represents a fully convex form, such as a circle) to measure roughness; the color scale shows radial distance of the fragment centroid relative to the drop center. Note in particular the low axial ratio for particles with large radial distances (the outer platey fragments).

and resulting speed of fracture propagation (31). In its simplest form, progressive crack bifurcation might be expected to produce fragments with a fractal size distribution (41–43) as a result of hierarchical fracture (38). That some PRD fragmentation studies produce exponential FSDs, commonly interpreted to reflect a (memoryless or random) Poisson process, is therefore surprising and attributed to the internal stress field itself (34, 38). The exponential form of the distribution provides a direct measure of the dominant size (L_D) of the distribution, which is related to slope (s) as $L_D = -1/s$ (44). Our data add another dimension to the discussion and raise questions about the relation between crack propagation, branching, the location of interior voids, and the rate of expansion into the confining medium.

Fracture Patterns Revealed by μCT Imaging

The spatial distribution of fractures can be assessed from μCT scans of fragmented drops (Fig. 5 *A*–*F*). We start by discussing epoxy-encased PRDs (PRD1 to -3) (*SI Appendix*, Fig. S2). Longitudinal sections through μCT scans of PRD2 (single void) (Fig. 5*A*) and PRD3 (multiple voids) (Fig. 5*B*) have near-linear fractures that extend outward from the tail end toward the head—that is, in the direction of fracture propagation (red arrows). These fractures terminate in the outermost glass because the epoxy prevented outward expansion and complete disintegration of the PRD. Within the drop, fractures often bifurcate, as observed in high-speed photography of explosive PRD fragmentation (4, 22). The longitudinal section of epoxy-encased PRD3 shows that cracks (as seen in two dimensions) tend to bifurcate at acute angles close to the outer compressive layer (Fig. 6*B*, yellow arrow), while bifurcating cracks in the PRD interior are more likely to form obtuse angles (Fig. 6*B*, turquoise arrow and *SI Appendix*, Fig. S2). Fractures controlled by interior voids, in contrast, are perpendicular to the void margin (white arrows in Fig. 5 *A* and *C*).

Gel-encased PRD4 shows similar fracture patterns, although obtaining a true longitudinal section is complicated by the concave form of the original PRD (Fig. 5 *D*–*F*). A striking feature of Fig. 5*D* is a longitudinal fracture from the tail that bifurcates to create a V-shaped "shadow zone" around the voids in the head (a similar feature can be seen in figure 12 of ref. 34, which is a PRD fragmented in Carbopol noted by ref. 38 to have the "typical consistency" of hair gel). Fractures propagate outward from the tail toward the head and intersect the droplet surface to form circumferential fractures (Fig. 5*E*, pink arrows) that were interpreted by Hooke (1665) to be complete conical fractures (Fig. 1). Interior fractures perpendicular to the central void create a crazy paving pattern on the basal surface (Fig. 5*F*). Visual inspection shows no tendency of small particles to be concentrated in the interior, as hypothesized by ref. 22. Instead, small particles are found throughout the sample where multiple fractures intersect (38).

Another important observation is that fragment shapes vary systematically with their position within the original PRD and reflect patterns of fracture propagation. The primary direction of fracture is from the (broken) tail toward the head and outward into the compressive layer. Fragments formed by these fractures are typically platey, with the smallest dimension a measure of the spacing between near-parallel fractures (Fig. 5*G* and *SI Appendix*, Fig. S4). Crack bifurcation increases both the number of individual fractures and the range of fragment shapes. Additional controls on fragment shape are imparted by changing stress fields caused by interior voids that create distinctly blocky fragments, often bordered by part of the void wall. This creates a stark contrast between the outer platey and inner blocky fragments, a contrast that we quantify by measuring two-dimensional (2D) particle shapes in horizontal cross-sections of the 2D scans (Fig. 5*H*, Dataset S1, and *SI Appendix*, Fig. S5). Here, the axial ratio measures the extent of fragment elongation, solidity measures fragment angularity (45), and color is scaled to the radial distance of the fragment centroid from the drop center.

Quench Granulation and the Surprising Effect of Bubbles

We also measured FSDs for samples that disintegrated during initial contact with water (80 to 90 g each of bubble-free and

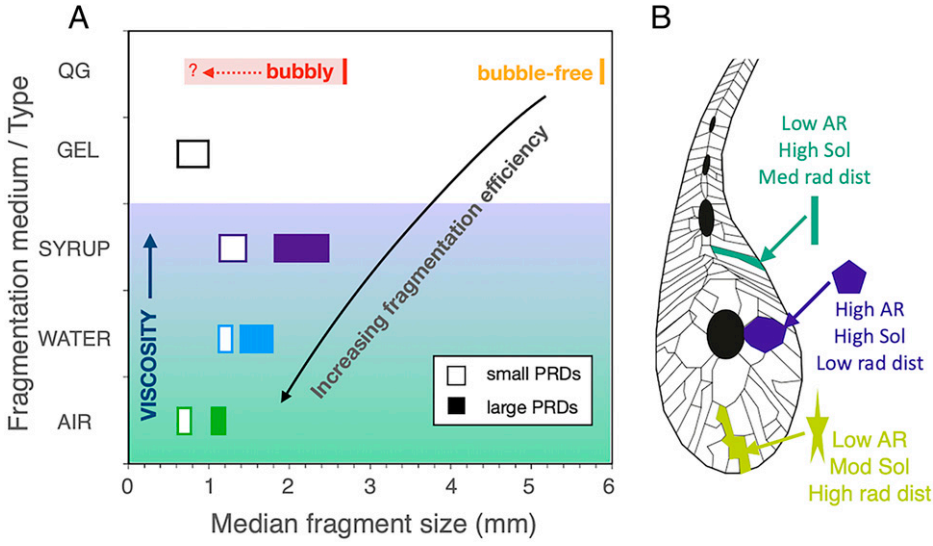

Fig. 6. Summary of PRD size and shape data. (*A*) Variation in median fragment size as a function of PRD size (small or large) and fragmentation conditions. Median grain size increases (fragmentation efficiency decreases) with increasing viscosity of the confining medium; hair gel range shows the effect of different assumptions of fragment shape. Quench granulation of bubble-free molten glass produces the largest fragments; explosive fragmentation in air produces the smallest fragments. Larger PRDs produce larger median fragments than small PRDs. Quench granulation of bubbly molten produces fragments with a limited size range that we hypothesize to be controlled by the interbubble spacing within the melt. (*B*) Sketch illustrating relation between fragment shape and location. AR, aspect ratio; Sol, solidity; rad dist, radial distance (colors and shape measurements as plotted in Fig. 5*H*).

bubble-bearing melt collected from multiple pours of ~20 g each). The comparison of FSDs from explosively fragmented PRDs and quench-granulated fragments is striking. Granulated fragments have median sizes that are larger than those of any explosively fragmented PRDs (Fig. 4*A*). Fragments formed by quench granulation of bubble-free molten glass have the largest median size (5.8 mm), the largest maximum size (>10 mm), and the smallest mass of particles <250 μm (<1% by mass). Fragments formed by quench granulation of bubbly molten glass have a median size of 2.7 mm, between those formed by quench granulation and explosive fragmentation of PRDs formed from bubble-free molten glass. The shape of the FSD also varies, with quench granulation of bubbly molten glass creating the most restricted size range; explosive PRD fragmentation in air produces the broadest size distribution.

Quench granulation of bubbly and bubble-free molten glass provides information on fragmentation by thermal stresses alone in the absence of stored residual stresses. Both yield FSDs that fit power laws with $D_m \sim 1.05$ (bubble free) to $D_m \sim 1.11$ (bubbly), which are similar to those determined by ref. 29 for explosively generated FSDs from lead crystal PRDs. The relatively large size of fragments produced by quench granulation of bubble-free melt is consistent with the lack of internal residual stresses; similar large fragment sizes are produced when PRDs are annealed or when the outer compressive layer is etched away by acid (22).

Perhaps more surprising is the effect of adding bubbles to the melt prior to quenching. Critically, bubble addition prevented PRD formation. In contrast to the voids that form during PRD cooling, which help to reduce tensional stresses in the PRD interior, steam-filled bubbles added to the melt prior to quenching will effectively increase the coefficient of expansion (contraction) of the melt–bubble mixture. Because the bubbles are not uniform in size and spacing, quenching will cause heterogeneous stress distributions because of differential contraction of the steam-filled bubbles and the melt. A corollary is that the FSD is modulated by the size and spacing of bubbles in the melt; the limited fragment size range suggests a fairly homogeneous bubble population.

Concluding Remarks

PRDs have long fascinated the materials science community because of their unusual properties, notably the strength of the head and the explosivity of the metastable interior. Our study of PRDs provides a different perspective by asking questions about the fragmentation environment, the relation between fracture processes and the fragments they produce, and the properties of the melt (bubble bearing or bubble free). This work also provides insight into processes that may operate during hydrovolcanic eruptions.

What Is the Effect of the Confining Medium on PRD Fragmentation? First and foremost, we demonstrate that the environment of fragmentation affects the FSD, such that fragmentation in air, water, and syrup creates FSDs with increasingly larger median sizes (Fig. 6*A*). The observed change in FSD with the properties of the surrounding medium is surprising and demonstrates that fragmentation is controlled not only by patterns of internal stress but also, by interactions of the fracture process with the confining medium. Another example of this phenomenon may be the differences in crack branching properties observed when borosilicate glass plates are fractured in water or dry nitrogen (46). Additionally, our results suggest that volcanic fragmentation caused by the interaction of magma (silicate melt) with water (8) or a water–sediment slurry (13) might produce fragments with different size populations.

What Do FSDs Tell Us about Explosive Fragmentation of PRDs? Published studies of PRD FSDs suggest that they fit either a power law (fractal, hierarchical) or exponential (random, Poisson process) distribution. The distinction is important for understanding the relation between patterns of fracture and the fragments that result from complex fracture networks. Our data suggest that explosive fragmentation of PRDs in air and water generates FSDs that are fractal over most of the mass distribution, with fractal dimension $1 < D_m < 2$. These D_m values reflect the dominance of small fragments relative to large fragments and provide a direct measure of fragmentation efficiency. Fractal size distributions are not surprising for rapidly propagating and bifurcating cracks, but the change in fractal dimension with confining medium suggests some degree of externally imposed control on branching patterns. The variability in FSDs among PRDs fragmented in the same medium further indicates that the overall particle morphology and the number, size, and distribution of internal voids reflect (nonrepeatable) differences in cooling rate and resulting patterns of fragmentation throughout an individual drop. FSDs produced by explosive fragmentation in syrup are better fit by an exponential distribution and differ from the power law distributions primarily in the low abundance of the smallest fragments, perhaps reflecting a lower fracture density (thus limiting the fracture intersections responsible for the smallest particles). Explosive fragmentation in hair gel produced an FSD with a small median size and bimodal distribution that could be fit by two exponential curves. It is difficult to generalize from this single experiment, but it is remarkable that the median size is similar to fragmentation in air and smaller than for the more viscous water and syrup. Hair gel is strongly shear thinning, but even at high shear rates, the apparent viscosity is more similar to water than air. It may be that elastic properties of the gel are important at the low-strain, high–shear rate conditions of an exploding PRD; the predominantly elastic rheology at low strains (until the gel network ruptures) extends to higher strains and stresses with increases in shear rate (47). Another complication in assessing FSD form is the difficulty in defining size. Sieving, for example, assigns anisotropic particles to size classes based on their intermediate diameter, which may differ significantly from the commonly assumed equivalency with the diameter of a volume-equivalent sphere (40).

FSDs could also, in theory, provide a measure of crack branching length (that is, the distance between bifurcation points), which has been related to the stored energy in the glass (33). There are many factors, however, that complicate interpretations of crack branching from FSDs. First, crack length distributions would require measurements of fragment long-axis length, while crack spacing may be better approximated by fragment short-axis length. Second, many fragments form by merging or crossing fractures (33). Third, we have shown that the environment of disintegration affects the FSD and by inference, patterns of fracture formation. Finally, the internal stress field that affects fracture behavior is heterogeneous and includes very high compressive stresses near the droplet exterior, high tensional stresses in the droplet interior, and radially asymmetric stresses caused by the internal void(s) (Fig. 3). Void location may also alter patterns of fracture propagation, as suggested for the anomalous air-fragmented FSD that had a void located at the junction between head and tail (*SI Appendix*, Fig. S1).

How Does Crack Propagation Affect Fragment Shape? Fragment shapes vary with location within the drop as a consequence of large stress changes from tensile in the interior to compressive in the outermost layer together with heterogeneous stress patterns around voids (Fig. 3). Changes in the geometry of the stress field affect crack bifurcation angles; large bifurcation angles in PRD interiors suggest equibiaxial pressure distributions, while small bifurcation angles toward the margin suggest uniaxial or torsional pressure distributions (33). Crack bifurcation angles, in turn, control the resulting fragment shapes (Fig. 5), such that interior fragments are blocky (bounded by oblique or right-angle fractures) and exterior fragments are elongate or platey (bounded by high-angle fractures) (Fig. 6*B*). Importantly, although patterns of fracture have been extensively studied in the glass industry (32, 33), less attention has been paid to the fragment shapes resulting from those fractures. Conversely, volcanologists use particle size and shape to infer fragmentation processes (48–50) but have not related shape to fracture processes. The range of shapes produced from fragmentation of a single PRD, however, suggests caution in assigning individual shapes to a specific fragmentation mechanism.

Insight into Quench Granulation. Two important results of our study are that 1) quench granulation produces larger fragments than explosive fragmentation and that 2) during quench granulation, the presence of bubbles in the molten glass affects not only the FSD but also, the ability of the melt to form PRDs at all. Quench granulation can occur if fractures form at flaws in the margin of the melt drop as it quickly cools and contracts in contact with water, preventing the formation of a strong shell of glass that is essential for generating PRDs. Fractures and fragments breaking off the drop margin will expose water to hotter material in the drop interior, causing fragmentation to propagate inward. The larger fragment size is therefore expected for quench granulation because the glass has lower stored elastic strain energy than a PRD, which has substantial residual tensile stress from contraction of the interior as it cooled within a solid shell of glass. In this way, the products of quench granulation are similar to those of annealed PRDs. The presence of heterogeneously distributed steam-filled bubbles in the molten glass likely enhances contraction on cooling and creates stress heterogeneities that induce failure of the glass near the water, preventing the formation of a strong outer shell of bubbly glass. The bubbles and associated stress heterogeneities in turn cause FSDs to be modulated by the original size and spacing of bubbles. Finally, the observation that bubble-bearing molten glass is prone to quench granulation has important implications for conditions of fragmentation in volcanic eruptions where (bubbly) magma interacts with groundwater, surface water, and/or sediment–water slurries (15, 19). Bubbles are generally not included in magma–water interaction laboratory experiments (48). Exceptions are the experiments in ref. 51, where water injected into hot permeable analog magma caused fragmentation by generation and expansion of steam within the pore space of the magma. In contrast, our experiments show that thermal granulation can be induced by heterogeneous stresses associated with isolated (suspended) bubbles that do not form connected porous networks.

Materials and Methods

Making PRDs. We made PRDs in two ways. We made small glass drops by melting the end of a glass rod using a glasswork torch to form a molten bulb ~10 mm in diameter and then allowing the droplet of molten glass to fall under gravity into a beaker of water at room temperature. We used soda lime glass rods ("clear transparent glass" from Bullseye Glass) with $SiO_2 \sim 70\%$ and a linear coefficient of explansion COE $= 9.1 \times 10^{-6}$ K^{-1}; this composition is similar to that used in the experiments in refs. 22, 34, and 37. The beaker was filled with ~500 mL of water, and the base was cushioned by torn cardboard to reduce the likelihood of drop disintegration on impact. These PRDs were examined photographically and used for μCT experiments. Drops that remained intact throughout quenching formed glass beads that weighed <1 g, measured 3 to 8 mm in diameter at the head, and tapered to a thin tail 0.5- to 2-mm thick (*SI Appendix*, Table S1). Many drops, however, disintegrated on contact with water, which frothed from steam generation. Disintegration occurred in a series of energetic fracture pulses rather than a single explosion; the vibrations of each phase of fracturing could be felt in the end of the rod to which the drops were still attached.

To construct larger PRDs, we turned to Bristol Blue Glass (https://bristol-glass.co.uk), which invited us to their studio. They use lead oxide glass (25% PbO, 5% Na_2O, 8% K_2O, 62% SiO_2; COE $= 7.5$ to 9×10^{-6} K^{-1}) as used in ref. 26. Intact glass drops weighed ~20bg each; we collected the large PRDs or fragments of drops that broke on contact with water (quench granulation). Bristol Blue Glass artists created bubbly molten glass by adding a potato to the furnace of molten glass, which liberates the high moisture content of the potato as steam (https://bernardkatz.com/potato-in-glass/). Although repeated attempts were made, they never succeeded in making an intact PRD from bubbly melt. Again, we collected the fragments formed during disintegration for size measurements and comparisons with PRD experiments.

Fragmentation Experiments. To explore controls on PRD fragmentation, we disintegrated both small and large glass drops by breaking their tails with pliers while the drops were immersed in air, water, and Tate and Lyle golden syrup (viscosity = 86 Pa s at 18 °C) (*SI Appendix*, Table S1). Fragments were then recovered by sieving; for the experiments in syrup, successive dilution of the syrup with water ensured recovery of the smallest particles. Postfragmentation PRD fragment sizes were measured using sieves at whole φ-sizes from -4φ to 4φ (where $\varphi = -\log_2 d$, where d is diameter in millimeters), such that -4φ to $4\varphi = 16$ to 0.64 mm (Dataset S1). Fragments produced by drops that disintegrated during formation were also sieved, with separate measurements made for those from pure and those from bubbly molten glass. An additional experiment involved breaking a PRD in hair gel (in essence a Carbopol dispersion neutralized with triethanolamine; made by Unilever). Grain size data for the gel experiment were determined from μCT images, with the measured volume of each fragment used to determine the cumulative volume distribution (= mass distribution because all fragments have the same density). In these measurements, we lack data from some of the tail, which was broken outside of the confining material. Comparison with sieve data requires the volume of each fragment to be converted to a linear size class. A common approach is to use the equivalent sphere diameter (34, 38). Inspection of the fragments shows, however, that they range in shape from blocky to platey, which has implications for comparison with sieve size data. For this reason, we convert volume to linear size assuming either cubic or tabular shapes. For the latter, we equate the sieve size to the intermediate axis (= long axis) of the assumed shape (40).

Imaging. We imaged PRDs in several different ways. They are transparent; therefore, photographic documentation allowed us to image the sizes, shapes, and spatial distribution of internal bubbles. A visual representation of the internal stress field was provided by adding cross-polarizing sheets to the imaging setup. The polarizers also showed that both glass fragments and void-free (or void-poor) epoxy-coated PRDs that remained intact after their tails were broken did not retain visible residual stresses.

To determine the three-dimensional geometry of fracture patterns, including the relation of fractures to both the outer compressive surface and the interior voids, we use μCT imaging. We ran four μCT experiments with small PRDs using a Nikon XTH 225ST laboratory scanner at the Rutherford Appleton Laboratory (Harwell) operating at 66 keV and 190 mA and using monochromatic X-rays (*SI Appendix*, Table S2). First, we embedded three PRDs in epoxy, two with and one without an interior void. We later imaged the void-bearing PRD fragmented in hair gel (in the previous section). In all cases, the tail was exposed so that it could be broken, leaving the PRD fragments in place for imaging (*SI Appendix*, Fig. S6). Each tomographic image is generated by rotating the PRD (embedded in epoxy or gel) in small steps around a single axis of rotation. We acquired

3,142 projections over 360° of rotation, each with an exposure time of 500 ms. To minimize beam-hardening artifacts, we placed a 0.1-mm aluminum filter in the beam path to attenuate low-energy X-rays. We reconstructed the scan data using filtered back-projection algorithms with a voxel size of ∼4.8 μm and analyzed the reconstructed image volumes in Avizo software (https://www.fei.com/software/amira-avizo/). μCT reconstructed volumes were first smoothed using a median filter; then, they were thresholded, segmented, and rendered to visualize individual fragments and analyze their volumetric size distribution. To test for fractal size distributions, we used the measured volume of 1,150 fragments (a total volume fraction of >0.999) (Dataset S1).

When embedded in epoxy, the void-bearing PRD fractured internally but maintained a thin intact surface layer of glass (Fig. 5 *A–C* and *SI Appendix*, Fig. S2), while the voidless PRD did not fracture. From this, we concluded that the epoxy was too strong to allow the expansion necessary for fracture propagation and fragment displacement. Hair gel, in contrast, allowed complete fracture and preserved the relative geometry of the fractured pieces while allowing sufficient fragment separation for imaging individual particle sizes and shapes.

The μCT data could also be viewed in two dimensions as successive slices. Viewing the data in this way allowed analysis of both apparent fracture angles and apparent shapes. Additionally, 2D shape analysis is widely used in volcanology. We assessed the angles empirically, as shown in Fig. 5 *A–F* and *SI Appendix*, Fig. S2. We measured fragment shape parameters from binary images, thresholded to distinguish between glass and epoxy, using ImageJ (https://imagej.nih.gov/ij/). We analyzed three horizontal cross-sections and one vertical cross-section of the gel-encased PRD (*SI Appendix*, Fig. S6), although curvature of the PRD made analysis of the longitudinal section challenging. For this reason, we use data only from the horizontal sections in the text (Fig. 5*H*). We define axial ratio as the ratio of the minor to major axes of the best-fit ellipse and solidity as the ratio of the particle area to the area of the convex hull; a perfect circle would have a value of one in both parameters, with decreasing values toward zero indicating increasing shape irregularity.

Data Availability. All study data are included in the article and/or supporting information.

ACKNOWLEDGMENTS. We thank L. Mastin for thoughtful review, Bristol Blue Glass for their assistance with making PRDs, Kate Dobson for extensive help with the μCT imaging, and the Royal Society for the opportunity to read Hooke's original PRD work. K.V.C. acknowledges support from the AXA Research Fund and the Royal Society Wolfson Research Merit Award.

1. L. Brodsley, F. C. Frank, J. W. Steeds, Prince Rupert's drops. *Notes Rec. R. Soc. Lond.* **41**, 1–26 (1986).
2. A. M. Roos, Thomas Philipot and chemical theories of the tides in seventeenth-century England. *Ambix* **48**, 125–136 (2001).
3. M. Dobre, On glass-drops: A case study of the interplay between experimentation and explanation in seventeenth-century natural philosophy. *J. Early Mod. Stud. (Bucur.)* **1**, 105–124 (2013).
4. W. Johnson, S. Chandrasekar, Rupert's glass drops: Residual-stress measurements and calculations and hypotheses for explaining disintegrating fracture. *J. Mater. Process. Technol.* **31**, 413–440 (1992).
5. S. Bless, Failure waves and their possible roles in determining penetration resistance of glass. *Int. J. Appl. Ceram. Technol.* **7**, 400–408 (2010).
6. D. J. Buchanan, T. A. Dullforce, Mechanism for vapour explosions. *Nature* **245**, 32–34 (1973).
7. R. S. Peckover, D. J. Buchanan, D. Ashby, Fuel–coolant interactions in submarine vulcanism. *Nature* **245**, 307–308 (1973).
8. K. H. Wohletz, Explosive magma-water interactions: Thermodynamics, explosion mechanisms, and field studies. *Bull. Volcanol.* **48**, 245–264 (1986).
9. R. Büttner, B. Zimanowski, Physics of thermohydraulic explosions. *Phys. Rev. E* **57**, 5726 (1998).
10. R. Büttner, P. Dellino, L. La Volpe, V. Lorenz, B. Zimanowski, Thermohydraulic explosions in phreatomagmatic eruptions as evidenced by the comparison between pyroclasts and products from Molten Fuel Coolant Interaction experiments. *J. Geophys. Res. Solid Earth* **107**, ECV-5-1–ECV 5-14 (2002).
11. E. P. Fitch, S. A. Fagents, Using the characteristics of rootless cone deposits to estimate the energetics of explosive lava–water interactions. *Bull. Volcanol.* **82**, 83 (2020).
12. P. Kokelaar, Magma-water interactions in subaqueous and emergent basaltic. *Bull. Volcanol.* **48**, 275–289 (1986).
13. J. D. L. White, Impure coolants and interaction dynamics of phreatomagmatic eruptions. *J. Volcanol. Geotherm. Res.* **74**, 155–170 (1996).
14. C. I. Schipper, J. D. L. White, Magma-slurry interaction in Surtseyan eruptions. *Geology* **44**, 195–198 (2016).
15. E. J. Liu, K. V. Cashman, A. C. Rust, A. Höskuldsson, Contrasting mechanisms of magma fragmentation during coeval magmatic and hydromagmatic activity: The Hverfjall Fires fissure eruption, Iceland. *Bull. Volcanol.* **79**, 68 (2017).
16. L. G. Mastin, Generation of fine hydromagmatic ash by growth and disintegration of glassy rinds. *J. Geophys. Res. Solid Earth* **112**, B02203 (2007).
17. L. G. Mastin, O. Spieler, W. S. Downey, An experimental study of hydromagmatic fragmentation through energetic, non-explosive magma–water mixing. *J. Volcanol. Geotherm. Res.* **180**, 161–170 (2009).
18. A. Schmid *et al.*, Experiments on the heat discharge at the dynamic magma-water-interface. *Geophys. Res. Lett.* **37**, L20311 (2010).
19. E. J. Liu, K. V. Cashman, A. C. Rust, S. R. Gislason, The role of bubbles in generating fine ash during hydromagmatic eruptions. *Geology* **43**, 239–242 (2015).
20. J. Van Otterloo, R. A. F. Cas, C. R. Scutter, The fracture behaviour of volcanic glass and relevance to quench fragmentation during formation of hyaloclastite and phreatomagmatism. *Earth Sci. Rev.* **151**, 79–116 (2015).
21. J. Snart, L. Physico-mechanical experiments and discussions of the phaenomena observable in that casual product of art the hand granade, Prince Rupert's drop, or glass tear. *Philos. Mag.* **22**, 334–339 (1805).
22. S. Chandrasekar, M. M. Chaudhri, The explosive disintegration of Prince Rupert's drops. *Philos. Mag. B Phys. Condens. Matter Struct. Electron. Opt. Magn. Prop.* **70**, 1195–1218 (1994).
23. H. Aben *et al.*, On the extraordinary strength of Prince Rupert's drops. *Appl. Phys. Lett.* **109**, 231903 (2016).
24. M. M. Chaudhri, Crack bifurcation in disintegrating Prince Rupert's drops. *Philos. Mag. Lett.* **78**, 153–158 (1998).
25. M. Chaudhri, Explosive disintegration of thermally toughened soda-lime glass and Prince Rupert's drops. *Eur. J. Glass Sci. Technol. B Phys. Chem. Glasses* **47**, 136–141 (2006).
26. M. Chaudhri, Self-sustained fracture waves in a lead oxide-silica glass. *J. Appl. Phys.* **110**, 013523 (2011).
27. M. Chaudhri, The role of residual stress in a Prince Rupert's drop of soda-lime glass undergoing a self-sustained and stable destruction/fracture wave. *Phys. Status Solidi A Appl. Mater. Sci.* **206**, 1410–1413 (2009).
28. M. Chaudhri, C. Liangyi, The catastrophic failure of thermally tempered glass caused by small-particle impact. *Nature* **320**, 48–50 (1986).
29. M. P. Silverman, W. Strange, J. Bower, L. Ikejimba, Fragmentation of explosively metastable glass. *Phys. Scr.* **85**, 065403 (2012).
30. M. Bochkov, D. Gusenkova, E. Glushkov, J. Zotova, S. N. Zhabin, Resistive method for measuring the disintegration speed of Prince Rupert's drops. *Eur. J. Phys.* **37**, 055707 (2016).
31. R. C. Bradt, The fractography and crack patterns of broken glass. *J. Fail. Anal. Prev.* **11**, 79–96 (2011).
32. D. Hull, *Fractography: Observing, Measuring and Interpreting Fracture Surface Topography* (Cambridge University Press, 1999).
33. G. Quinn, *NIST Recommended Practice Guide: Fractography of Ceramics and Glasses*, 3rd ed. (National Institute of Standards and Technology, Gaithersburg, MD, 2020).
34. G. van Dalen, S. A. Kooij, "Micro-CT imaging and analysis of the fragmentation of Prince Rupert's glass drops" in *Micro-CT User's Meeting* (Ghent, Belgium, 2018).
35. D. Gusenkova, Resistive method for measuring the disintegration speed of Prince Rupert's drops. arXiv [Preprint] (2016). https://arxiv.org/abs/1602.06801 (Accessed 28 July 2020).
36. E. M. Aster *et al.*, Reconstructing CO_2 concentrations in basaltic melt inclusions using Raman analysis of vapor bubbles. *J. Volcanol. Geotherm. Res.* **323**, 148–162 (2016).
37. J. S. Pallister *et al.*, Faulting within the Mount St. Helens conduit and implications for volcanic earthquakes. *Bulletin* **125**, 359–376 (2013).
38. S. Kooij, G. van Dalen, J.-F. Molinari, D. Bonn, Explosive fragmentation of Prince Rupert's drops leads to well-defined fragment sizes. *Nat. Commun.* **12**, 2521 (2021).
39. D. L. Turcotte, Fractals and fragmentation. *J. Geophys. Res. Solid Earth Planets* **91**, 1921–1926 (1986).
40. H. M. Buckland *et al.*, Measuring the size of non-spherical particles and the implications for grain size analysis in volcanology. *J. Volcanol. Geotherm. Res.* **415**, 107257 (2021).
41. H. J. Herrmann, Patterns and scaling in fracture. *Phys. Scr. T* **38**, 13–21 (1991).
42. J. Åström, J. Timonen, Fragmentation by crack branching. *Phys. Rev. Lett.* **78**, 3677 (1997).
43. P. Kekäläinen, J. A. Aström, J. Timonen, Solution for the fragment-size distribution in a crack-branching model of fragmentation. *Phys. Rev. E Stat. Nonlin. Soft Matter Phys.* **76**, 026112 (2007).
44. K. V. Cashman, B. D. Marsh, Crystal size distribution (CSD) in rocks and the kinetics and dynamics of crystallization II: Makaopuhi lava lake. *Contrib. Mineral. Petrol.* **99**, 292–305 (1988).
45. E. J. Liu, K. V. Cashman, A. C. Rust, Optimising shape analysis to quantify volcanic ash morphology. *GeoResJ* **8**, 14–30 (2015).
46. D. P. DeLellis, N. A. Mecholsky, J. J. Mecholsky Jr., G. D. Quinn, A fractal analysis of crack branching in borosilicate glass. *J. Am. Ceram. Soc.* **103**, 5283–5290 (2020).
47. R. R. Fernandes, D. E. Andrade, A. T. Franco, C. O. Negrão, The yielding and the linear-to-nonlinear viscoelastic transition of an elastoviscoplastic material. *J. Rheol.* **61**, 893–903 (2017).
48. T. Dürig *et al.*, A new method for the determination of the specific kinetic energy (SKE) released to pyroclastic particles at magmatic fragmentation: Theory and first experimental results. *Bull. Volcanol.* **74**, 895–902 (2012).
49. T. Dürig *et al.*, Deep-sea fragmentation style of Havre revealed by dendrogrammatic analyses of particle morphometry. *Bull. Volcanol.* **82**, 1–20 (2020).
50. E. P. Fitch, S. A. Fagents, Characteristics of rootless cone tephra emplaced by high-energy lava–water explosions. *Bull. Volcanol.* **82**, 62 (2020).
51. R. Trigila, M. Battaglia, M. Manga, An experimental facility for investigating hydromagmatic eruptions at high-pressure and high-temperature with application to the importance of magma porosity for magma-water interaction. *Bull. Volcanol.* **69**, 365–372 (2007).